AIAA JOURNAL
Vol. 38, No. 7, July 2000

Direct Numerical Simulation of Leading-Edge Receptivity to Sound

David Fuciarelli,* Helen Reed,† and Ian Lyttle‡
Arizona State University, Tempe, Arizona 85287-6106

Numerical simulations of leading-edge acoustic receptivity are performed for a flat plate with a modified-super-elliptic leading edge. For small freestream amplitude the agreement between branch I receptivity coefficients predicted from the direct numerical simulation (DNS) and the experiments for acoustic waves at zero incidence is excellent. The effect of angle of incidence of the impinging wave is investigated and found to produce higher receptivity coefficients than in the symmetric case. The slope of leading-edge receptivity coefficient vs angle of incidence of the impinging wave is found to be less than $\frac{1}{4}$ of the slope predicted by zero-thickness flat-plate theory. However, there is excellent agreement between the DNS and finite-nose-radius theory. These results clearly demonstrate the importance of including the effects of the finite nose radius in any receptivity study. Finally, downstream of the leading-edge region linear stability theory is found to reproduce accurately the characteristics of the instability waves. At higher freestream forcing, an instability wave generated by nonlinear interaction is found at double the frequency of the forcing.

I. Introduction

TRANSITION in wall-bounded shear layers occurs because of an incipient instability of the basic flowfield, which depends intimately on subtle, and sometimes obscure, details of the flowfield. In other words, the wall-bounded shear layer is an open system. Disturbances in the freestream, such as sound or vorticity, enter the boundary layer as steady and/or unsteady fluctuations of the basic state. This part of the process, called receptivity, provides the vital initial conditions of amplitude, frequency, and phase for the breakdown of laminar flow.[1–5]

External disturbances common to the flight environment are typically either acoustic or vortical. For a given frequency neither acoustic waves nor vortical disturbances contain a wavelength that coincides with the instability generated within the boundary layer. Thus in this case some mechanism for transferring energy from a much longer wavelength wave to a relatively small wavelength instability wave must exist. Therefore a proper understanding of the receptivity process will include proper characterization of the external disturbance environment, as well as an understanding of both the mechanisms for the transfer of energy among different wavelengths and the effects of different disturbance environments. Detailed studies will also show how different geometries affect the process and how fluid properties such as Reynolds number and Mach number affect receptivity. Characterization of the external environment includes the wavelength and frequency spectrum of incoming disturbances. For acoustic waves the orientation of the acoustic wave with respect to the geometry is an important characteristic. For vortical disturbances the orientation, i.e., streamwise, normal, or spanwise or some combination, and the amplitude all play a role.

Theoretical investigations into acoustic receptivity have identified mechanisms for the transfer of energy among disparate wavelengths. In the research of Goldstein,[6] receptivity to acoustic waves impinging upon a flat-plate geometry at zero angle of incidence was investigated. Referring to Fig. 1, the primary mechanism for transferring energy is the relatively rapid growth of the mean boundary layer and the associated pressure gradients near the stagnation point. The investigations were performed using the linearized unsteady boundary-layer equation (LUBLE), which is a parabolic equation and therefore conducive to less costly numerical methods. Energy from the external disturbance environment is transferred to streamwise decaying eigenfunctions whose wavelength decreases as the flow progresses downstream. Thus, a process by which long wavelengths become shorter wavelengths is found in these so-called Lam–Rott eigenfunctions.[7] The Lam–Rott eigenfunctions match onto the high-Reynolds-number approximation to the linear instability wave solution (i.e., the Tollmien–Schlichting wave solution) farther downstream[6]; therefore, if one knows the amplitude of the Lam–Rott eigenfunction, the amplitude of the instability wave downstream is known. Goldstein et al.[8] and Heinrich and Kerschen[9] calculated leading-edge receptivity coefficients for various freestream disturbances. Goldstein[10] and Goldstein and Hultgren[11] also showed that discontinuities in slope or curvature in the geometry also provide a mechanism for acoustic receptivity. Regions where surface irregularities exist promote small-scale variations of the mean-flow boundary layer, and therefore the mechanism is very similar to the flat-plate case with no surface irregularity.

The preceding results apply to a zero-thickness flat plate. Hammerton and Kerschen[12,13] extend the analysis to account for a finite-thickness and curved leading edge by considering a parabolic geometry. The analysis is formulated to provide insight into the effect of nose radius, an effect present in any manufacturable geometry. The Mach number and the amplitude of the impinging acoustic disturbance are considered to be small so that the mean-flow pressure field can be computed with incompressible theory. The mean flow is two-dimensional and symmetric. Lam and Rott[14] generalized their eigenfunctions to account for arbitrary streamwise variation in the mean flow, and Hammerton and Kerschen[12] show that their expressions are in agreement with these more general results. The relevant parameter is the Strouhal number based on the nose radius St_r. The results of this work show that the receptivity coefficient is nearly unity when the nose radius is zero and decreases dramatically with increasing nose radius. The receptivity coefficient is shown to increase with increasing angle of incidence of the acoustic wave. Hammerton and Kerschen[13] consider the small-Strouhal-number limit. For freestream acoustic waves at zero incidence, the receptivity is found to vary linearly with Strouhal number, giving a small increase in the receptivity coefficient relative to that for the flat-plate case. However, for oblique waves the receptivity varies with the square root of the Strouhal number, leading to a sharp decrease in the amplitude of the receptivity coefficient compared to the flat-plate case.

Received 18 November 1998; revision received 4 November 1999; accepted for publication 12 November 1999. Copyright © 2000 by the American Institute of Aeronautics and Astronautics, Inc. All rights reserved.

*Ph.D. Graduate, Department of Mechanical and Aerospace Engineering. Student Member AIAA.

†Professor, Department of Mechanical and Aerospace Engineering; helen.reed@asu.edu. Associate Fellow AIAA.

‡Ph.D. Candidate, Department of Mechanical and Aerospace Engineering; lyttle@asu.edu.

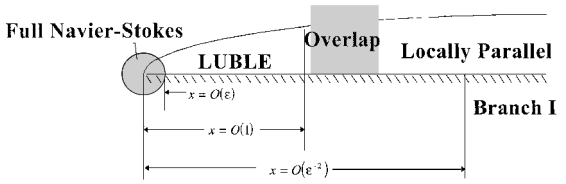

Fig. 1 Regions of validity for disturbance equations. Here $\varepsilon = F^{1/6}$, where $F = \omega\nu/U^2$, U is the freestream speed, and ω is the frequency of the acoustic wave.[6]

A leading edge with finite curvature and thickness has been shown to produce instability waves. Experiments in leading-edge receptivity have shown that great care must be taken in order to produce results that are comparable to theory and numerical simulation.[15] The very small amplitudes upstream are not detectable in the experiments, and the instability waves can only be measured after significant growth has occurred. However, once the amplitude of an instability wave has been determined downstream, one can use linear stability theory (LST) to provide amplitudes in the leading-edge region.

Numerical simulations of receptivity have provided a database of results that clarify issues in receptivity and can be used to refine experimental procedures. One of the most important results is that the amplitudes of the generated instability waves scale linearly with the acoustic forcing amplitude when the forcing amplitude is less than 1% of the freestream speed.[16] Receptivity caused by surface irregularities or discontinuities in curvature such as those that exist when an ellipse is joined to a flat plate has been accurately simulated.[16] When the curvature discontinuity at the juncture of an ellipse and a flat plate is removed, the instability wave amplitudes decrease by more than half. Numerical simulations have also affirmed that smaller nose radii produce larger leading-edge instability-wave amplitudes.[17] Recent developments[18] have shown promise for the investigation of receptivity in three-dimensional flows, which is likely to be quite different from two-dimensional flows.

II. Numerical Method

In the research presented here the focus is upon acoustic waves impinging upon an elliptic-type leading edge joined to a flat plate. Numerical simulations are conducted to examine the effect of angle of incidence, frequency, and amplitude of the incoming acoustic wave. The simplified geometry lends itself to comparison with experimental and theoretical investigations while retaining the geometric properties, pressure gradients, and mean-flow boundary-layer adjustment that promote the wavelength conversion necessary for receptivity to occur. The discontinuity at the juncture of the ellipse and the flat plate is eliminated by using a modified super ellipse (MSE) in order to concentrate on the effects of the finite-curvature and finite-thickness leading edge. All of the simulations are for two-dimensional incompressible mean flows and disturbance solutions. The research presented here focuses on the effects of different disturbance environments by varying the properties of the impinging acoustic wave. It is hoped that by clarifying these effects that the understanding of the receptivity process is enhanced and the results provide a basis for further investigation.

The two-dimensional incompressible Navier–Stokes equations are cast in a stream-function/vorticity form and solved in a general-curvilinear-coordinate system using the Modified Strongly Implicit Procedure (MSIP).[19] The disturbance equations are formulated by assuming a solution composed of a linear combination of the steady basic state and a time-dependent perturbation.

The geometry of interest is an MSE[16] leading edge attached to a flat plate. The MSE is given by

$$(1 - x/AR)^{2+(x/AR)^2} + y^2 = 1 \qquad (1)$$

where lengths have been nondimensionalized with the half-thickness of the plate. Examining this equation, at $x = 0$ (upstream-most point of the geometry) the exponent is the same as a normal ellipse and becomes cubic as we approach the flat-plate juncture at $x = AR$. This variation allows for continuous curvature at the flat-plate/leading-edge juncture. Therefore the receptivity mechanism predicted by Goldstein[10] and Goldstein and Hultgren[11] and found by Lin et al.[16] at a point of discontinuous curvature will not be present in the simulations, thus allowing the focus to be on the leading edge.

Both a hyperbolic orthogonal and a body-intrinsic grid generator were formulated. The body-intrinsic scheme generated a grid that was just as orthogonal as the hyperbolic generator to within the truncation error of the hyperbolic scheme. Because the body-intrinsic generator was more computationally efficient in both CPU time and RAM, it was used to generate the grids. Grid points were densely clustered near the surface and leading edge of the geometry.

Proper selection of boundary conditions is important for the numerical solution of the governing equations. On the solid-surface boundary no-slip and no-penetration conditions are imposed. The far-field boundary conditions are imposed as velocity boundary conditions. For the basic-state calculations the inviscid values of velocity are computed from a panel code. For the disturbance calculations a time-periodic velocity fluctuation is imposed. By doing so we model the acoustic wave as an infinite-wavelength disturbance. This near-field condition assumes that the wavelength of the acoustic wave is much longer than the extent of the computational domain, which is true when the Mach number is sufficiently small.

As a result, for the disturbance equations a truncated Fourier expansion in time is then assumed for the perturbation. The expansion is made in multiples of the forcing frequency. This results in a coupled set of nonlinear steady complex equations. The advantage with this set of equations is that it does not require marching the solution forward in time as would be required with the usual time-dependent equations. The solutions are brought to steady state, and solutions for all time are retrievable by recomposing the Fourier series. The Fourier expansion in time also lends itself to a coarse-grain parallelism.

When traveling waves are present, the solution may be corrupted by the waves reflecting off an ill-posed outflow boundary. The buffer-domain technique used is similar to that of Mittal and Balachandar.[20] In this technique the streamwise diffusion terms in the vorticity-transport equation are multiplied by a coefficient that exponentially decays to zero with increasing streamwise distance within a buffer zone appended to the domain downstream. The coefficient has the form

$$f_{BZ} = \exp[-\gamma(\hat{x})^{\beta}], \qquad \hat{x} = \frac{\cosh(x) - \cosh(x_0)}{\cosh(x_e) - \cosh(x_0)} \qquad (2)$$

where x_0 and x_e represent the streamwise locations of the beginning and end of the buffer domain, respectively. The buffer-zone parameters used in these simulations were $\gamma = 40.0$ and $\beta = 1.4$. This technique causes the vorticity-transport equation to become convectively dominated in the streamwise direction within the buffer domain. Solutions within this buffer domain are not physically correct. The length of the buffer domain L_{BZ} is typically on the order of two to four disturbance wavelengths. In following sections studies are shown that ensure the solution is independent of the length of the domain and the buffer-zone parameters.

The outflow-boundary conditions were chosen to be compatible with the buffer-zone technique. The second derivatives of the dependent variables with respect to the streamwise direction were set to zero. For the basic-state calculations no buffer zone was necessary because the solution has no traveling waves that could reflect from the outflow boundaries. However, to ensure compatibility with the disturbance equations, the buffer zone was implemented in the basic state and found to have no discernible effect on either the basic-state or the disturbance solution.

III. Results

Acoustic leading-edge receptivity on an MSE connected to a flat plate is investigated by direct numerical simulation (DNS). The effects of frequency, forcing amplitude (both linear and nonlinear), and angle of incidence of the impinging acoustic wave are investigated.

Unless otherwise indicated, the simulations are conducted around the baseline case of a 1) 6:1 MSE at Reynolds number 2.4×10^3 based on plate half-thickness L and freestream speed U, 2)

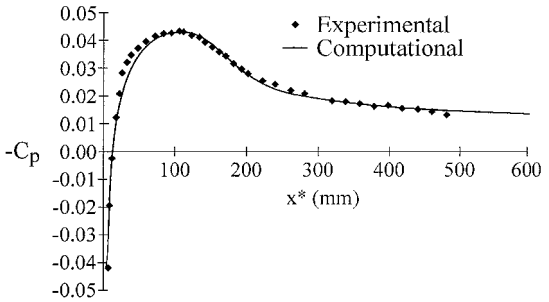

Fig. 2 Comparison of computationally and experimentally determined pressure coefficient for 40:1 MSE (experiment: Saric and White[21]).

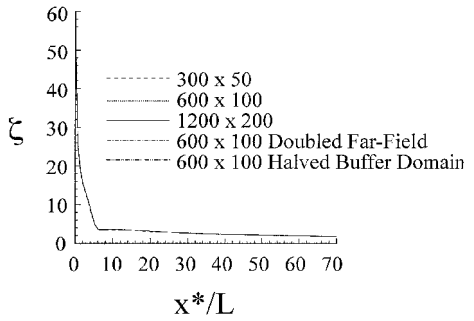

Fig. 3 Wall vorticity for different grids and far-field and outflow-boundary locations: $Re = 2.4 \times 10^3$, 6:1 MSE.

freestream forcing amplitude normalized with U of $A_{ac} = 1\%$, and 3) nondimensional frequency of $F = 86 \times 10^{-6}$ ($F = \omega\nu / U^2$, and ω is acoustic-wave frequency).

A. Basic-State Solutions

A typical C-grid was used with the grid clustered toward the surface and also toward the stagnation point. Care was taken to ensure that the grid had no discontinuities in the metric coefficients. Computing the term ($\xi_x \eta_x + \xi_y \eta_y$), which is zero for an orthogonal grid, shows that a maximum value of 2.41×10^{-5} was attained near the stagnation point for a 600×100 grid. This value decreased with increasing grid sizes.

The inviscid flowfield was computed using a doublet panel code. The code does not impose a Kutta condition and therefore is invalid for plates that produce lift. A comparison of the pressure coefficient with the experiments of Saric and White[21] on a 40:1 MSE is shown in Fig. 2. The excellent agreement between the experimentally measured pressure coefficient and the numerically determined coefficient is caused by the extensive care taken in the experiment to provide a comparison with the numerical simulations.

The basic-state solution is computed using the full two-dimensional incompressible Navier–Stokes equations in a general-curvilinear-coordinate system. Grid studies were performed to ensure that convergence of the correct solution has been achieved. Figure 3 shows the basic-state wall vorticity as a function of x for a 6:1 MSE at a Reynolds number of 2.4×10^3 for different grid sizes. Here the basic-state stagnation point is located at $x = 0$ and $y = 0$, and the juncture of the MSE and the flat plate is located at $x = 6$ and $y = 1$. The basic-state solution with a grid size of 600×100 is indistinguishable from the 1200×200 grid-size solution (to within the truncation error of the 1200×200 grid). The rapid rise of wall vorticity near the stagnation point is well resolved, and the wall vorticity approaches the Blasius values downstream in the flat-plate region of the flow. The location of the far-field boundary has been investigated to ensure that the solution is independent of its location. A distance of 10 units from the surface of the plate was found to be acceptable for the far-field boundary.

B. Disturbance Calculations

The disturbance calculations were performed using the MSIP method. Because the equations are a set of steady, complex equations, care must be taken to ensure that no spurious wave reflections from the outflow boundary are present. In addition, because the amplitudes of the instability waves near branch I have small amplitude, one must ensure that the waves are adequately resolved by proper grid studies and examinations of the truncation error.

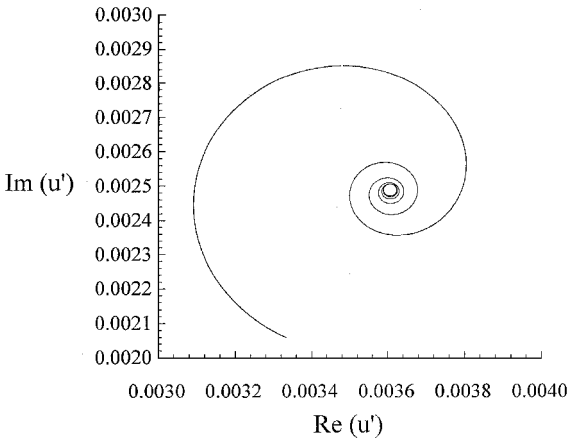

Fig. 4 Complex polar plot of Fourier coefficient of streamwise velocity.

1. *Decomposition Technique*

The solution of the disturbance equations contains both a Stokes-wave solution and an instability wave. Because we are interested in the transfer of energy from the acoustic wave to the instability wave, it is necessary to separate these two solutions by taking advantage of the differences between them. The Stokes-wave solution has a very long wavelength and much higher phase speed as compared to the instability wave. Wlezien[22] proposed the following method for decomposing these two solutions:

1) Decompose the time-domain solution into a Fourier coefficient. For the solutions presented here this step has already been performed. If one were running an unsteady code, then sampling over several time periods must be performed.

2) Sample points over several instability wavelengths in the streamwise direction at a constant height from the plate. For these calculations streamwise velocity was the sampled quantity because it is typically the quantity measured in the experiments.

3) At each streamwise location calculate the relative phase and amplitude and plot in the complex plane. A representative plot of this step is shown in Fig. 4.

Because the phase and amplitude of the Stokes wave are relatively constant over several wavelengths of the instability wave, decomposition is possible. A vector drawn to the center of the spiral shown in Fig. 4 represents the amplitude and phase of the Stokes wave. The decaying spiral (in this case, because the locations are upstream of branch I of the neutral stability curve) represents the amplitude and phase of the instability wave. By computing the radius of curvature, one may extract the amplitude of the instability wave as a function of the streamwise distance. In addition, derivatives of the phase in the streamwise direction give the wave number. Accurate decomposition of the instability wave depends on the phase and amplitude variations of the Stokes wave being much smaller than those of the instability wave.

Near the stagnation point it is not the case that the phase and amplitude of the Stokes wave are relatively constant in the streamwise direction. Local pressure gradients caused by the finite thickness and curvature of the leading edge modulate the amplitude and phase of the Stokes wave in such a way as to be indistinguishable from the variation of the instability wave, and therefore this decomposition technique fails in this region.

2. *Linear Calculations*

In earlier numerical investigations for small forcing amplitudes, the linearized disturbance equations are the proper governing equations. The advantage in using the linearized disturbance equations is that they are significantly simpler to solve than the nonlinear disturbance equations because the equations may be solved for single-mode solutions.

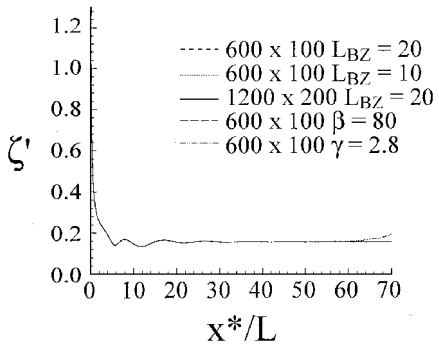

Fig. 5 Disturbance wall vorticity for different grids and buffer-zone parameters. x^* is dimensional streamwise location: $F = 86 \times 10^{-6}$, $Re = 2.4 \times 10^3$, 6:1 MSE.

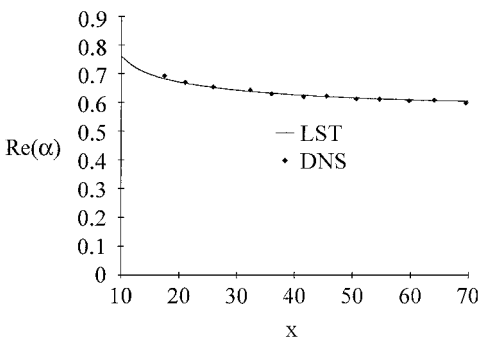

Fig. 6 Comparing wave numbers from DNS and LST: $F = 86 \times 10^{-6}$, $Re = 2.4 \times 10^3$, 6:1 MSE.

The simulations performed here are done with the following goals in mind:

1) Provide comparisons with LST to ensure that the solution retains the correct physics.

2) Investigate the effect of incidence angle on receptivity in order to compare with the findings of Heinrich and Kerschen[9] and Hammerton and Kerschen.[12]

Symmetric calculations. For most of the calculations in this section, a planar acoustic wave impinging upon a 6:1 MSE at zero incidence angle is simulated. The Reynolds number in these cases was 2.4×10^3, corresponding to the experimental conditions of Saric and White[21]: a freestream speed of 8.6 m/s with a plate half-thickness of 4.8 mm.

Grid studies were performed to ensure that the solution was resolved. The length of the buffer domain was varied to ensure the solution was independent of this parameter. Also, the buffer-zone parameters were varied to ensure their independence. Figure 5 shows the disturbance wall vorticity for several grid sizes, buffer-domain lengths, and buffer-domain parameters. Once again the solutions contain only negligible differences between the 600×100 and the 1200×200 grid. The buffer zone length of 20 units is found to be adequate for preventing wave reflection in this case. The location of the beginning of the buffer domain is $x_0 = 80.0$.

At the frequencies modeled the branch I locations of the neutral stability curve are within the buffer region. Because solutions are not physical in the buffer region, LST is used to extrapolate the receptivity coefficients to their values at branch I. Because this technique is used, it is important to show that the solutions downstream are in fact governed by LST. The growth rates were computed from theory using the numerically determined basic state. Derivatives of the decomposed phase were taken to find the wave numbers in the numerical solutions. Comparisons of wave numbers and growth rates between DNS and LST are shown in Figs. 6 and 7. As can be seen from the figures, the wave numbers and growth rates are well predicted by LST downstream of the leading edge. Comparisons further upstream in the leading-edge region are problematic because the decomposition technique itself breaks down there.

Branch I receptivity coefficients were obtained for a range of frequencies. For example, the values obtained for both a 6:1 and 20:1 MSE are contained in Table 1; the 20:1 geometry is included for comparison with the experiments of Saric and White.[21] The receptivity coefficient K_I here is defined as the amplitude of the instability wave at branch I of the neutral stability curve divided by the amplitude of the incident acoustic wave. The receptivity coefficients have been extrapolated downstream from the numerical results by using LST. The amplitude of the instability wave was taken at its maximum absolute value within the boundary layer after decomposing using the method just presented. Within the limited range of frequency sampled, the results of the numerical simulations show no significant variation. The agreement between the computations and the experiment is excellent, and we conclude that each validates the other.

Table 1 Branch I receptivity coefficients for multiple frequencies as predicted by DNS and compared with the experiments of Saric and White[21]

	K_I		
$F \times 10^6$	6:1 MSE DNS	20:1 MSE DNS	20:1 MSE experiment
80	0.0030	——	——
82	0.0030	0.048	0.050
84	0.0031	0.048	0.050
86	0.0032	0.048	0.050
88	0.0033	——	——
90	0.0034	——	——

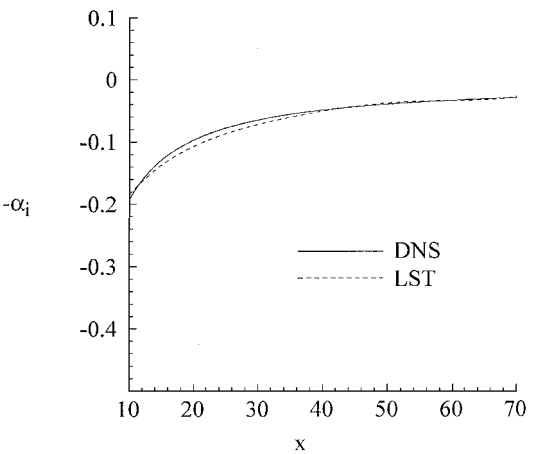

Fig. 7 Comparing growth rates from DNS and LST: $F = 86 \times 10^{-6}$, $Re = 2.4 \times 10^3$, 6:1 MSE.

The results of Haddad and Corke[17] show that the leading-edge receptivity coefficient has a value of approximately 0.47 for a Strouhal number of 0.01, based on the nose radius (which is the value in the present numerical simulations). In the theoretical results of Hammerton and Kerschen,[12] the leading-edge receptivity coefficient is found to be nearly unity. In the present simulations the value of the receptivity coefficient at an x location ($x = 4.8$) of $\frac{1}{2}$ the wavelength of the associated instability wave (which represents a distance based on the hydrodynamic length scale U/ω of approximately unity) compares well with the theoretical results, predicting a leading-edge value of approximately 0.75. Here LST was applied to the basic-state solutions upstream of $x = 10$ and growth rates integrated to estimate the receptivity coefficient at $x = 4.8$. Note that $x = 10$ is downstream of the juncture, although care was taken in the use of the MSE to provide continuous curvature there.

Observation. In trying to do these comparisons for leading-edge receptivity coefficients, certain difficulties arise. Uncertainty exists in the DNS (and experiments) in the choice of streamwise location in the leading-edge region at which the amplitude should be sampled for comparison with the asymptotic theory. Moreover it is often difficult to make direct leading-edge measurements in an experiment because of the scales involved and to separate the Stokes wave from the instability in the DNS in the leading-edge area because both exhibit variation on similar streamwise length scales.

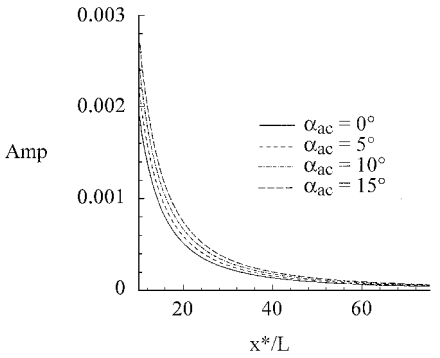

Fig. 8 Amplitudes of decomposed disturbance for different angles of incidence (α_{ac} in degrees) of acoustic wave: $F = 86 \times 10^{-6}$, $Re = 2.4 \times 10^3$, 6:1 MSE.

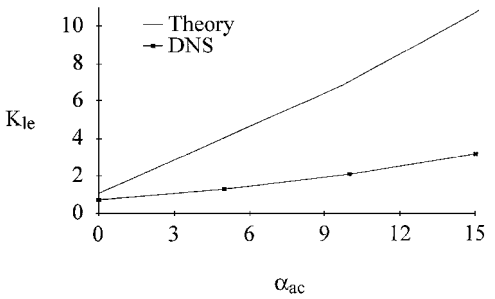

Fig. 9 Leading-edge receptivity coefficient as function of acoustic angle of incidence (in degrees). Theoretical results of Heinrich and Kerschen[9] are for zero-thickness flat plate at freestream Mach number $M = 0.01$. DNS results are for $F = 86 \times 10^{-6}$, $Re = 2.4 \times 10^3$, 6:1 MSE.

Consequently, in the present DNS we extrapolated LST forward to $x = 4.8$ for the qualitative comparison. These problems are removed when the receptivity coefficient is based on branch I results, as is seen in the preceding paragraph describing the straightforward and quantitative comparison between DNS and the experiments. Branch I is unambiguous, and we recommend that the standard definition of receptivity coefficient be based on it, especially to aid the community in the evaluation of different theories and numerical and experimental methods in the prediction of receptivity.

Nonsymmetric calculations. Acoustic waves impinging upon the plate at angles of incidence α_{ac} were investigated. The numerical far-field boundary condition in the disturbance calculation is modified to include a normal component of the velocity oscillation. This effectively changes the angle of incidence of the impinging acoustic wave. The basic-state solution remains at zero angle of attack. Because the flowfield is no longer symmetric, the full domain must be computed. An oblique acoustic wave causes small-amplitude motion of the stagnation point and thus introduces a small vertical component of velocity at the leading edge. The far-field boundary location and buffer-zone parameters are systematically varied to show invariance of the numerical solution.

The amplitudes of the instability waves are decomposed from the Stokes-wave solution in an identical manner as the preceding symmetric calculations. Figure 8 depicts the change in amplitude as the angle of incidence of the acoustic wave is increased. The decay of the instability is nearly the same as the zero-incidence case and is well predicted by LST in regions downstream of the leading edge.

Values of the leading-edge receptivity coefficient for different angles of incidence are determined and plotted in Fig. 9. Once again, the decomposition technique is not valid in this region, and the amplitudes are found by extrapolating using LST. The nondimensional wavelength (based on the half-thickness of the MSE) is approximately 10. Plotted in this same figure are the results of Heinrich and Kerschen.[9] As can be seen, there is an increase in the receptivity coefficient with increasing angle of incidence but at a much smaller rate than that predicted by this theory for the zero-thickness flat plate. The slope of the increase in receptivity for the DNS is approximately 0.15, whereas that predicted by Heinrich and Kerschen is approximately 0.65. Therefore the DNS predicts a slope of less than $\frac{1}{4}$ of the slope predicted by this theory.

A comparison with the finite-nose-radius theoretical results of Hammerton and Kerschen[12] shows much more encouraging results. The Strouhal number based on nose radius for the present simulations is 0.01, and Hammerton and Kerschen[13] point out that the asymptotic results for small Strouhal number do not apply. Because we are dealing with very low Mach numbers, the results for reduced acoustic frequency

$$k = \omega b / c \ll 1 \tag{3}$$

are applied. Here b is the airfoil semichord, and c is the speed of sound. In other words, the acoustic wavelength is long not only compared to the hydrodynamic length scale U/ω, but also compared to the airfoil chord. From Eqs. (4.3) and (4.9) in Hammerton and Kerschen,[12] the leading-edge receptivity coefficient is defined as

$$C_1(St_r, \alpha_{ac}) = \cos\alpha_{ac} C_s(St_r) + a^{\frac{1}{2}} \sin\alpha_{ac} C_a(St_r) \tag{4}$$

Here C_s and C_a are the symmetric and antisymmetric components of the receptivity coefficient, and $a = \omega b / U$ is the aerodynamic reduced frequency. For the present geometry and freestream conditions $U/\omega = 4.8$ in units of plate half-thickness, and $St_r = 0.01$ based on nose radius. From Figs. 4 and 5 of Hammerton and Kerschen,[12] the following values are predicted:

$$|C_s| = 1, \qquad \arg C_s = 0.67\pi$$
$$|C_a / C_s| = 4.9, \qquad \arg(C_a / C_s) = 0.2\pi \tag{5}$$

It is difficult for us to determine a precise value for a because our geometry is semi-infinite in the downstream direction. Per Hammerton and Kerschen[12] the following condition must be satisfied in order that their local expansion of the thickness distribution for an airfoil with a rounded leading edge of radius r_n be valid:

$$b/L = \mathcal{O}(L/r_n) \tag{6}$$

Satisfying the strict equality of Eq. (6) puts our trailing edge far downstream at $x = 40$ in units of half-thickness (away from the influence of the leading edge) and suggests the calculation be done for a value of $a = 4.1$. This value gives the comparison shown in Table 2. The agreement is excellent for the range of small incidence angles investigated (0–15 deg) and (comparing with the poor agreement in Fig. 9) clearly demonstrates the importance of including the effects of the finite nose radius in any receptivity study. (A comparison with Haddad and Corke[17] is not possible because, not only was their wave at incidence, but also their basic state.) Our definition of a was because our geometry was semi-infinite and would need to be verified for larger incidence angles. Also, to study higher incidence angles (up to 180 deg) would likely necessitate the use of a finite body.

3. *Nonlinear Calculations*

In the nonlinear simulations for large-amplitude A_{ac} freestream disturbances, a master-slave parallel virtual machine code is used to generate solutions more efficiently. The coarse-grain parallelism present in the Fourier-decomposed disturbance equations lends itself well to computers with a small number of very large processors in a shared-memory environment. Grid-convergence studies are performed, and the number of frequencies was doubled to ensure the solution was independent of the number of frequencies (see Fig. 10).

Table 2 Leading-edge receptivity coefficients for various incidence angles as predicted by DNS and compared with the finite-nose-radius theory of Hammerton and Kerschen[12]

α_{ac}, deg	C_1 DNS	C_1 theory
0	0.75	1.0
5	1.3	1.8
10	2.1	2.6
15	3.2	3.4

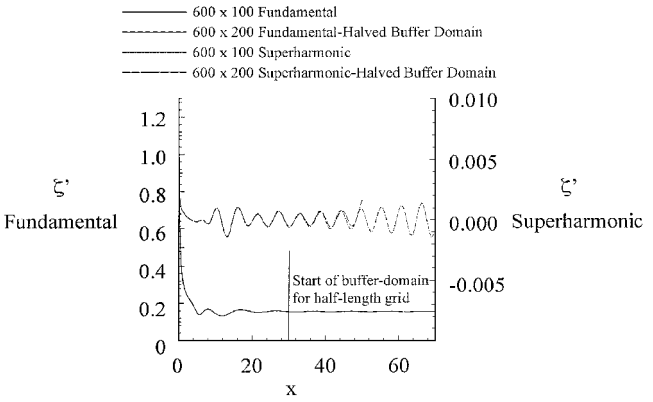

Fig. 10 Disturbance wall vorticity for fundamental frequency and superharmonic on two different grids: $F = 86 \times 10^{-6}$, $Re = 2.4 \times 10^3$, $A_{ac} = 1\%$, $\alpha_{ac} = 0$ deg, 6:1 MSE.

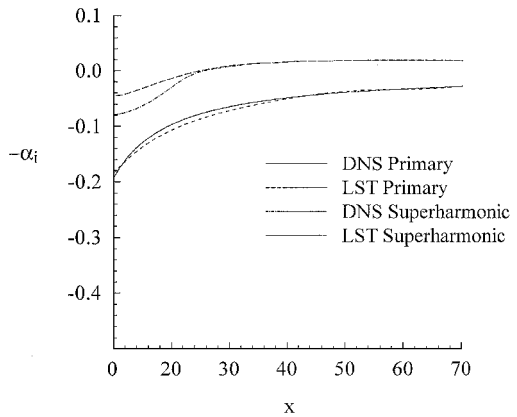

Fig. 11 Growth rates from DNS compared with LST for nonlinear calculations: $F = 86 \times 10^{-6}$, $Re = 2.4 \times 10^3$, $A_{ac} = 1\%$, $\alpha_{ac} = 0$ deg, 6:1 MSE.

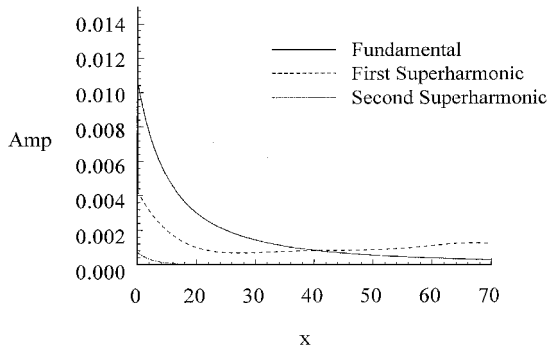

Fig. 12 Streamwise Fourier amplitude at nonlinear forcing amplitude of 5.0%: $F = 86 \times 10^{-6}$, $Re = 2.4 \times 10^3$, $A_{ac} = 5\%$, $\alpha_{ac} = 0$ deg, 6:1 MSE.

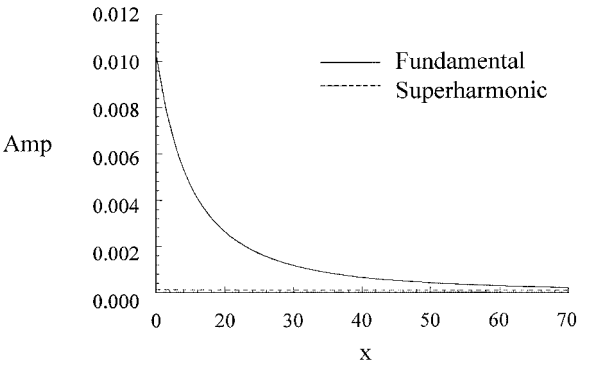

Fig. 13 Streamwise Fourier amplitude at nonlinear forcing amplitude of 0.5%: $F = 86 \times 10^{-6}$, $Re = 2.4 \times 10^3$, $A_{ac} = 0.5\%$, $\alpha_{ac} = 0$ deg, 6:1 MSE.

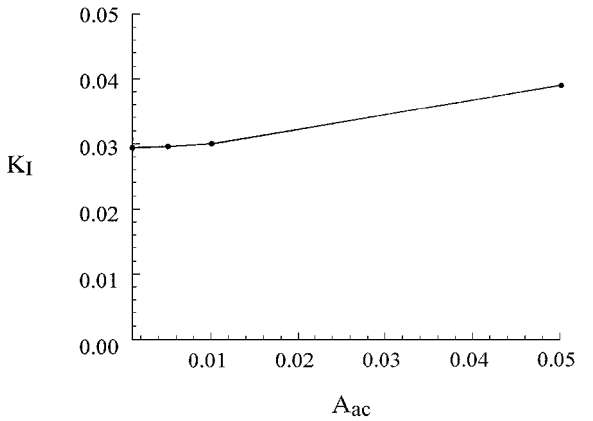

Fig. 14 Branch I receptivity coefficients as function of forcing amplitude. $F = 86 \times 10^{-6}$, $Re = 2.4 \times 10^3$, $\alpha_{ac} = 0$ deg, 6:1 MSE.

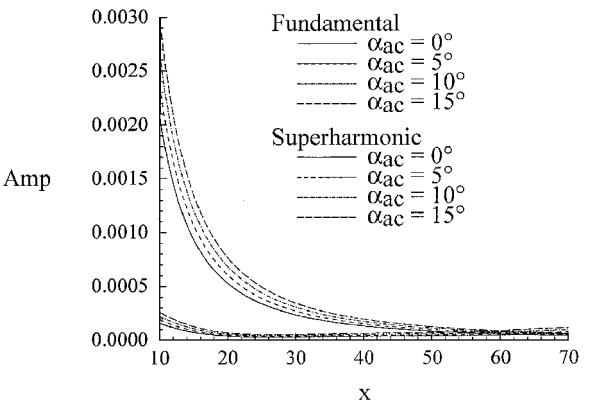

Fig. 15 Streamwise Fourier amplitude at nonlinear forcing amplitude of 1.0% for different angles of incidence of acoustic wave: $F = 86 \times 10^{-6}$, $Re = 2.4 \times 10^3$, $A_{ac} = 1\%$, 6:1 MSE.

At 1% freestream forcing and zero angle of incidence, an instability wave generated by nonlinear interaction was found at double the frequency of the forcing. This superharmonic was found to grow at the branch I location ($x = 25$) predicted by LST for the doubled frequency (Fig. 11). The amplitude of the superharmonic was $\mathcal{O}(10^{-4})$, which corresponds to the square of the forcing amplitude. However, because the fundamental-frequency solution decays in the computational domain and the superharmonic grows, the superharmonic dominated the fundamental-frequency solution in a region downstream of the leading edge. Further downstream, for these experimental conditions the superharmonic decayed again (branch II at $x = 83$) and had negligible amplitude at the branch I location ($x = 95$) of the fundamental-frequency instability wave.

At 5% forcing and zero angle of incidence, a second superharmonic is present but rapidly decays in the streamwise direction (Fig. 12). The solutions for 0.1 and 0.5% forcing amplitudes were computed, and they differed negligibly from the linear simulations (Fig. 13).

A summary of branch I receptivity coefficients as a function of forcing amplitude is shown in Fig. 14. Again, the receptivity coefficient is defined as the amplitude of the instability wave at branch I normalized by the amplitude of the incident acoustic wave. A weak nonlinearity is observed at 1% forcing. At 5% forced there is pronounced nonlinear interaction.

The effect of angle of incidence of the acoustic wave was investigated for the amplitudes of 1 and 5% (Figs. 15 and 16). In these simulations only the fundamental frequency was forced, and the angle of incidence of the acoustic wave was simulated by imposing a vertical component of oscillating velocity at the far field. The results indicate the same trends as those of the linear calculations; enhanced receptivity occurs at nonzero angles of incidence. Also,

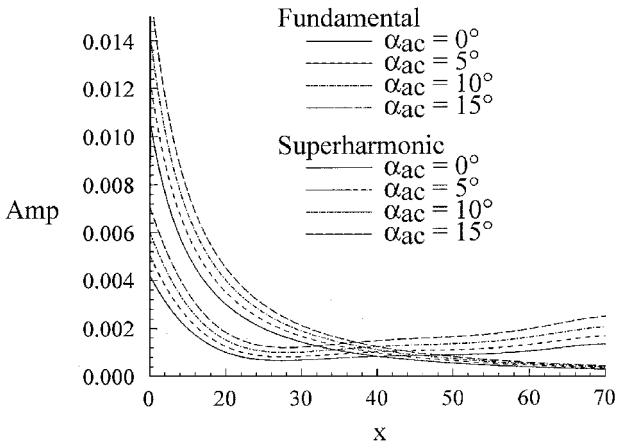

Fig. 16 Streamwise Fourier amplitude at nonlinear forcing amplitude of 5.0% for different angles of incidence of acoustic wave: $F = 86 \times 10^{-6}$, $Re = 2.4 \times 10^3$, $A_{ac} = 5\%$, 6:1 MSE.

higher amplitudes are found for the superharmonics at the nonzero angles of incidence.

IV. Conclusions

Numerical simulations of leading-edge acoustic receptivity are performed for a flat plate with an MSE leading edge. For small freestream amplitude the agreement between branch I receptivity coefficients predicted from the DNS and the experiments of Saric and White[21] for acoustic waves at zero incidence is excellent. The effect of angle of incidence of the impinging wave is investigated and found to produce higher receptivity coefficients than in the symmetric case. The slope of leading-edge receptivity coefficient vs angle of incidence of the impinging wave is found to be less than $\frac{1}{4}$ of the slope predicted by zero-thickness flat-plate theory. However, there is excellent agreement between the DNS and finite-nose-radius theory of Hammerton and Kerschen.[12] These results clearly demonstrate the importance of including the effects of the finite nose radius in any receptivity study. Finally, downstream of the leading-edge region, LST is found to reproduce accurately the characteristics of the instability waves.

Nonlinear interactions for the particular freestream and geometry conditions simulated appear at forcing amplitudes greater than about 1%. The 1% forcing condition corresponds to nearly 120 dB for the experiments performed in the Arizona State University Unsteady Wind Tunnel. It is hard to imagine a flight condition where acoustic levels of this magnitude would be present. However, these (and much higher) levels are present in turbine engines, and the results can indicate trends for use in investigating transition in these environments. Moreover, at the higher Reynolds numbers of flight, branch I for the various frequency solutions may be located in adverse-pressure-gradient regions near the leading edge, and disturbances created by lower-amplitude forcing can provide a richer content for the transition process. This along with the enhanced receptivity at angle of incidence indicates a possible role for nonlinearity at the lower-amplitude forcing characteristic of flight.

Acknowledgments

This work was supported at various stages by the Air Force Office of Scientific Research and NASA Langley Research Center.

References

[1]Morkovin, M. V., "On the Many Faces of Transition," *Viscous Drag Reduction*, Plenum, New York, 1969, pp. 1–31.

[2]Reshotko, E., "Environment and Receptivity," *Special Course on Stability and Transition of Laminar Flows*, von Kármán Inst., AGARD Rept. 709, Rhode-St.-Genese, Belgium, March 1984, pp. 4-1–4-11.

[3]Goldstein, M. E., and Hultgren, L. S., "Boundary-Layer Receptivity to Long-Wave Freestream Disturbances," *Annual Review of Fluid Mechanics*, Vol. 21, 1989, pp. 137–166.

[4]Kerschen, E. J., "Boundary Layer Receptivity Theory," *Applied Mechanics Review*, Vol. 43, No. 5, Pt. 2, 1990, pp. 152–157.

[5]Saric, W. S., Reed, H. L., and Kerschen, E. J., "Leading-Edge Receptivity to Sound: Experiments, DNS, Theory," AIAA Paper 94-2222, June 1994.

[6]Goldstein, M. E., "The Evolution of Tollmien-Schlichting Waves near a Leading Edge," *Journal of Fluid Mechanics*, Vol. 127, 1983, pp. 59–81.

[7]Lam, S. H., and Rott, N., "Theory of Linearized Time-Dependent Boundary Layers," Cornell Univ. Graduate School of Aerospace Engineering, U.S. Air Force Office of Scientific Research, Rept. TN-60-1100, Ithaca, NY, July 1960.

[8]Goldstein, M. E., Sockol, P. M., and Santz, J., "The Evolution of Tollmien-Schlichting Waves near a Leading Edge. Part 2. Numerical Determination of Amplitudes," *Journal of Fluid Mechanics*, Vol. 129, 1983, pp. 443–453.

[9]Heinrich, R. A., and Kerschen, E. J., "Leading-Edge Boundary Layer Receptivity to Various Freestream Disturbance Structures," *Zeitschrift für Angewandte Mathematik und Mechanik*, Vol. 69, No. 6, 1989, pp. T596–T598.

[10]Goldstein, M. E., "Scattering of Acoustic Waves into Tollmien-Schlichting Waves by Small Streamwise Variations in Surface Geometry," *Journal of Fluid Mechanics*, Vol. 154, 1985, pp. 509–529.

[11]Goldstein, M. E., and Hultgren, L. S., "A Note on the Generation of T-S Waves by Sudden Surface-Curvature Change," *Journal of Fluid Mechanics*, Vol. 181, 1987, pp. 519–525.

[12]Hammerton, P. W., and Kerschen, E. J., "Boundary-Layer Receptivity for a Parabolic Leading Edge," *Journal of Fluid Mechanics*, Vol. 310, 1996, pp. 243–267.

[13]Hammerton, P. W., and Kerschen, E. J., "Boundary-Layer Receptivity for a Parabolic Leading Edge. Part 2. The Small Strouhal Number Limit," *Journal of Fluid Mechanics*, Vol. 353, 1997, pp. 205–220.

[14]Lam, S. H., and Rott, N., "Eigen-Functions of Linearized Unsteady Boundary Layer Equations," *Journal of Fluids Engineering*, Vol. 115, No. 4, 1993, pp. 597–602.

[15]Saric, W. S., "Physical Description of Boundary Layer Transition: Experimental Evidence," *Special Course on Progress in Transition Modeling*, Rept. 793, AGARD, March–April 1993, pp. 1-1–1-51.

[16]Lin, N., Reed, H. L., and Saric, W. S., "Effect of Leading Edge Geometry on Boundary-Layer Receptivity to Freestream Sound," *Instability, Transition, and Turbulence*, Springer–Verlag, New York, 1992, pp. 421–440.

[17]Haddad, O., and Corke, T. C., "Boundary Layer Receptivity to Freestream Sound on Parabolic Bodies," *Journal of Fluid Mechanics*, Vol. 368, 1998, pp. 1–26.

[18]Collis, S. S., and Lele, S. K., "Receptivity to Surface Roughness near a Swept Leading Edge," *Journal of Fluid Mechanics*, Vol. 380, 1999, pp. 141–168.

[19]Schneider, G. E., and Zedan, M., "A Modified Strongly Implicit Procedure for the Numerical Solution of Field Problems," *Numerical Heat Transfer*, Vol. 4, No. 1, 1981, pp. 1–19.

[20]Mittal, R., and Balachandar, S., "Direct Numerical Simulation of Flow past Elliptic Cylinders," *Journal of Computational Physics*, Vol. 124, No. 2, 1996, pp. 351–368.

[21]Saric, W. S., and White, E. B., "Influence of High-Amplitude Noise on Boundary-Layer Transition to Turbulence," AIAA Paper 98-2645, June 1998.

[22]Wlezien, R. W., "Measurement of Acoustic Receptivity," AIAA Paper 94-2221, June 1994.

P. J. Morris
Associate Editor